RSC Advances

REVIEW

View Article Online
View Journal | View Issue

Cite this: *RSC Adv.*, 2025, **15**, 18893

From waste to functional materials: advances in porous material synthesis and applications derived from coal gasification slag

Mengdan Huo,[ab] Changjiang Huang,[ab] Anqi Guo,[ab] Jianbo Zhang[c] and Jian-ming Gao *[ab]

Coal gasification slag (CGS) is a hazardous industrial byproduct generated during coal gasification process. Its large-scale accumulation leads to environmental pollution and wasting of land resources. Addressing these challenges, the development of high-value utilization strategies for CGS has become a critical priority in sustainable resource management. CGS has unique pore structure and high reactivity of alumina–silica components, enabling it to be transformed into porous materials, which offers the possibility for high-value utilization. This review systematically consolidates recent progress in designing and functionalizing CGS-based porous materials. First, we elucidate the microstructural and physicochemical properties of CGS, focusing on pore hierarchy, elemental distribution, and phase evolution. Next, we critically analyze mainstream synthesis methodologies, spanning acid/alkali etching, physical activation, and hybrid approaches for hierarchical structuring. Furthermore, we point out emerging applications across environmental and energy sectors, such as multifunctional adsorption (heavy metals, organics, CO_2), polymer nanocomposites, and electromagnetic shielding. Finally, we identify persistent challenges, including energy-intensive activation processes, synergistic utilization of different elements in CGS, and industrial scalability gaps, while proposing targeted solutions such as externally-coupled activation and full-component resource recovery. These insights aim to bridge fundamental research with industrial implementation, advancing CGS valorization toward a zero-waste paradigm.

Received 31st March 2025
Accepted 26th May 2025

DOI: 10.1039/d5ra02243f

rsc.li/rsc-advances

1. Introduction

As the core pathway for clean conversion of coal,[1,2] coal gasification technology transforms organic matter within coal into syngas feedstocks, including H_2, CO, and CH_4, *via* gasification reactions occurring under high-temperature and high-pressure conditions. This process concomitantly produces solid wastes such as coal gasification slag (CGS).[3,4] The annual production of CGS has surged dramatically with the large-scale development of gasification equipment.[5–7] The accumulation of CGS results in the inefficient utilization of land resources and poses environmental risks, such as leachate pollution and dust diffusion.[8–10] Consequently, the development of CGS resource technology is imperative to mitigate these adverse effects and facilitate the green transformation of the coal industry.

Presently, the primary utilization of CGS revolves around conventional building materials, such as cement, concrete, and non-fired bricks.[11–13] However, due to the carbon content constraints of raw materials, coarse slag components are predominantly employed in practical applications. In contrast, residual carbon (RC) in fine slag, characterized by low calorific value and high moisture content (typically exceeding 30%), necessitates the use of drying equipment during co-combustion, thereby compromising economic viability.[14,15] Although CGS holds potential in soil improvement, attributed to mineral elements like phosphorus, potassium, and silicon,[16,17] and preliminary research is underway for high-value applications such as rubber-plastic fillers[18] and ceramic materials,[19] the lack of technological maturity hinders large-scale implementation. Hence, the current scenario of substantial CGS stockpiles coupled with low utilization rates underscores the urgent need for novel utilization strategies.

The physicochemical properties of CGS are significantly influenced by gasification processes and coal types.[20–22] From the perspective of gasification processes,[23] in fixed-bed gasification, where the reaction is relatively mild and the gas–solid

[a]*Institute of Resources and Environment Engineering, State Environmental Protection Key Laboratory of Efficient Utilization Technology of Coal Waste Resources Shanxi University, Taiyuan 030006, P. R. China. E-mail: gaojianming@sxu.edu.cn*

[b]*Shanxi Key Laboratory of High-value Recycling of Coal-based Solid Waste, Shanxi Laboratory for Yellow River, Shanxi University, Taiyuan, 030006, China*

[c]*CAS Key Laboratory of Green Process and Engineering, National Engineering Laboratory for Hydrometallurgical Cleaner Production Technology, Institute of Process Engineering, Chinese Academy of Sciences, Beijing, 100090, China*

contact is insufficient, CGS contains high carbon content, with large mineral crystals and small specific surface area. In fluidized-bed gasification, the reaction is vigorous with good gas–solid contact, resulting in reduced carbon content in the CGS, the emergence of new mineral phases, and relatively well-developed pores. In entrained-flow gasification, where the reaction is nearly complete, the CGS is predominantly in glassy state with a very low carbon content, fine particle size, large specific surface area, and abundant pores. Regarding coal types,[24] brown coal-derived CGS has low carbon content, simple mineral composition, fine particle size, but underdeveloped pores. Bituminous coal-derived CGS exhibits complex ash composition, wide particle size distribution, and pore structure that is greatly affected. Anthracite-derived CGS contains high amount of fixed carbon, has stable minerals, large particle size, and an unsatisfactory pore structure. These differences in properties lead to variations in the reactivity of CGS, thereby affecting the performance and reproducibility of the products. However, these issues can be addressed by pre-treating the CGS to adjust its surface properties, optimizing the synthesis process parameters, and reasonably blending CGS from different sources.

Coal gangue (CG), fly ash (FA), and CGS are common coal-based solid wastes.[25,26] Rich in SiO_2 and Al_2O_3, they serve as raw material basis for the synthesis of porous materials.[27–29] However, CG exhibits low reactivity and needs pre-treatment through high-temperature calcination or chemical activation to enhance its reactivity.[30] Additionally, due to its uneven particle size distribution, CG requires crushing and classification processes,[31] which increase the cost and complexity of porous material synthesis. The impurities in FA are significantly influenced by combustion conditions. When combustion is incomplete, unburned carbon, iron, calcium, and other highly reactive impurities react with the synthesis system, generating impurity phases.[32,33] This process reduces the purity and quality of the resulting porous materials. In contrast, CGS offers unique advantages in the synthesis of porous materials. The residual carbon present within CGS can act as synthesis template, facilitating the regulation of pore structure.[34,35] Furthermore, the gasification process removes portion of sulfur compounds and carbonaceous materials,[3] thereby improving selectivity of synthesis process and purity of final products. Therefore, CGS is regarded as a relatively suitable raw material for the synthesis of porous materials.

This review article synthesizes the research advancements in CGS-based porous materials and elucidates the influence mechanisms of their physicochemical properties on the synthesis and application of such materials. The first section outlines the generation process and fundamental properties of CGS. The second section summarizes the methodologies for fabricating porous materials from CGS and critically evaluates preparation techniques, including acid etching, alkali activation, physical activation and hierarchical synthesis. The third section delineates the resource utilization approaches for CGS-based porous materials and explores their applications in heavy metal ion adsorption, organic pollutant adsorption, CO_2 capture, polymer composite reinforcement, and electromagnetic wave absorption. Finally, addressing existing challenges,

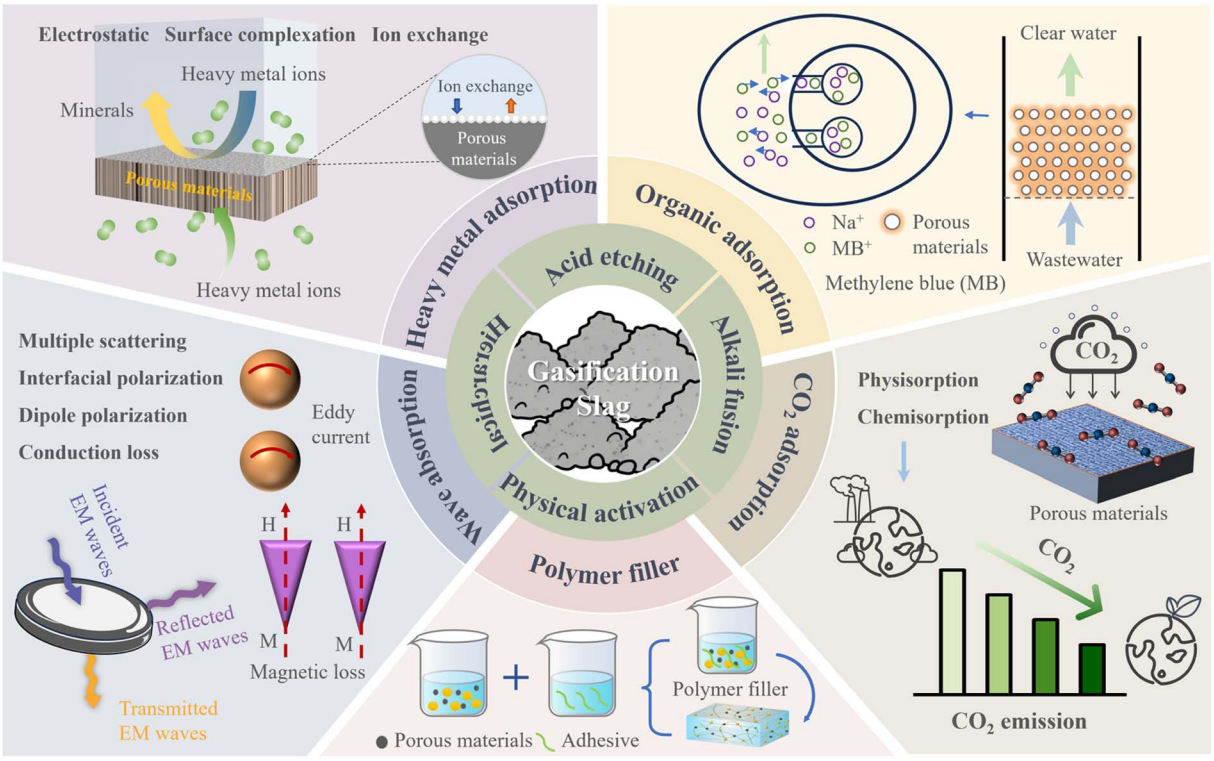

Fig. 1 Preparation technology and resource utilization of CGS-based porous materials.

this work proposes strategies such as low-energy activation and synergistic utilization of metallic and non-metallic elements to advance the multi-scenario large-scale application of CGS, thereby providing theoretical underpinnings for the comprehensive utilization of coal by-products (Fig. 1).

2. Generation and basic properties of CGS

2.1 CGS formation

During the coal gasification process, raw coal or coal coke undergoes incomplete combustion reactions with gasification media, including water vapor, oxygen (or air), and hydrogen, under high-temperature conditions (typically >1300 °C). Fixed carbon is converted into combustible gases, primarily comprising CO, H_2, and CH_4.[36,37] The solid waste generated is classified into coarse gasification slag (CGCS) and fine gasification slag (CGFS) based on the discharge location.[38,39] CGCS deposits directly at the bottom of the gasifier, presenting as lumps or granules with particle sizes predominantly in the range of 3.75–9 mm, accounting for 60–80% of the total CGS by volume.[40,41] CGFS is entrained as fly ash with the raw syngas and exits the furnace top. It is collected after water quenching and cyclone separation, with particle sizes <50 μm, constituting 20–40% of the total slag volume.[42,43] The formation processes of CGCS and CGFS are illustrated in Fig. 2a.

Due to kinetic limitations during gasification, incomplete conversion of carbon particles occurs due to the imbalance between surface reaction rates and internal diffusion rates, leading to the retention of RC. The unreacted carbon cores are subsequently encapsulated by molten silico–aluminate mineral phases generated during gasification, forming characteristic core–shell structured particles (as depicted in Fig. 2b). This structure imparts layered or honeycomb-like porous morphology to the RC particles, which exhibit high specific surface areas and open pore channels. These features provide active interfaces for mass transport and chemical reactions, serving as critical structural units for modulating the functional properties of CGS. CGCS undergoes prolonged high-temperature melting (>1400 °C) promoting near-complete carbon conversion (RC <10%). Conversely, CGFS retains a higher proportion of unreacted carbon (RC up to 20–40%) due to rapid cooling.[44]

2.2 CGS basic characteristics

CGS represents a complex system comprising inorganic mineral phases and RC. The mineralogical composition is primarily characterized by amorphous aluminosilicate glass phases (>50% by volume), intergrown with quartz, calcite, and mullite crystals.[21] Chemically, this material is defined by a silicoaluminate framework, with major oxides including SiO_2 (30–50%), Al_2O_3 (15–30%), CaO (5–15%), and Fe_2O_3 (3–8%).[45,46] The oxide distribution exhibits pronounced acidity, with SiO_2 + Al_2O_3 + Fe_2O_3 exceeding 70% and basic oxides (CaO + MgO + Na_2O + K_2O) contributing less than 30%.[47] These proportions are critically dependent on feedstock coal properties, operating temperatures, gasification agents, and other process variables.[8]

RC exhibit layered or honeycomb-like porous structure with specific surface area exceeding 200 $m^2\ g^{-1}$. The carbon core is chemically bonded to an aluminosilicate shell, forming highly reactive interface that facilitates mass transport. The synergistic interaction between surface functional groups (*e.g.*, –OH, –COOH) and trace impurities (*e.g.*, S, N, Fe, Ca) enhances the reactivity of RC and optimizes its pore structure.[48] This integration of structural and functional attributes enables RC to play pivotal role in the functional modification of CGS. By regulating pore architecture and surface chemistry, RC improves the performance of CGS-derived materials in applications such as wastewater treatment and gas adsorption. Table 1 demonstrates process-dependent variations in glass content

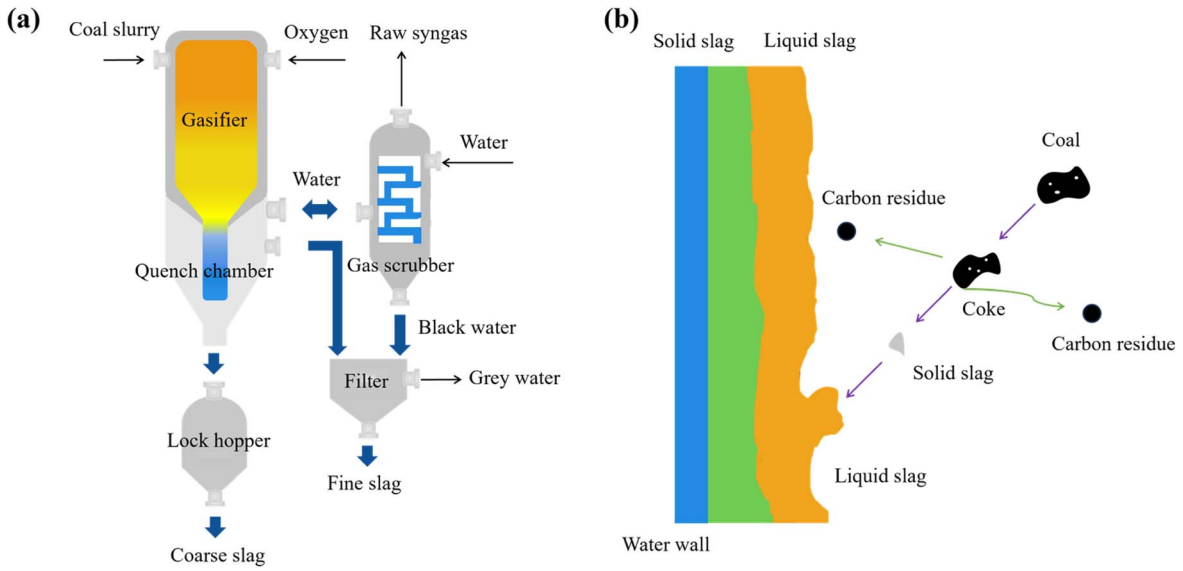

Fig. 2 (a) Schematic diagram of CGS generation. (b) Formation process of RC.

Table 1 Typical mineralogical composition of CGS

Furnace type	Slag type	Mineral composition	RC content (wt%)	Ref.
Opposed multi-burner gasification technology	CGFS	Mainly amorphous phase, containing a small amount of quartz	12.1	40
Opposed multi-burner gasification technology	CGCS	Mainly amorphous phase, containing a small amount of quartz	7.7	40
Texaco gasification technology	CGFS	Mainly amorphous phase, containing a small amount of quartz, augite, feldspar	30	49
Texaco gasification technology	CGCS	Mainly amorphous phase, containing a small amount of quartz, augite, feldspar	2.15	49
Opposed four-burner gasification technology	CGFS	Mainly amorphous phase, containing a small amount of quartz, calcite	16.2	50
Opposed four-burner gasification technology	CGCS	Mainly amorphous phase, containing a small amount of quartz, orthoclase, calcite, clay minerals	2.09	50
Former Texaco gasification technology	CGFS	Mainly amorphous phase, containing a small amount of quartz, calcite	37.55	50
Former Texaco gasification technology	CGCS	Mainly amorphous phase, containing a small amount of quartz, pyrite, calcite, clay minerals	2.23	50
Gaskombimat Schwarze Pumpe gasification technology	CGFS	Mainly amorphous phase, containing a small amount of quartz, pyrite, calcite, clay minerals	34.09	50
Gaskombimat Schwarze Pumpe gasification technology	CGCS	Mainly amorphous phase, containing a small amount of quartz, calcite, clay minerals	3.89	50
Half waste heat boiler technology	CGCS	Mainly amorphous phase, containing a small amount of quartz, mullite	9.51	51

and RC morphometry across gasifier types, underscoring the dominant influence of operational parameters on slag characteristics.

3. Preparation methods of CGS-based porous materials

Given the pronounced variability in CGS physicochemical attributes (encompassing mineralogical composition, residual carbon content, and pore architecture), conventional unitary preparation protocols are inadequate for accommodating feedstock diversity. Consequently, CGS characteristic-specific preparation methods have emerged as a research focus. Currently, four common preparation methods are acid etching, alkali activation, physical activation, and hierarchical synthesis.

3.1 Acid etching method

The acid etching technique involves the reaction of concentrated acids (*e.g.*, HCl, HAc) with metallic oxides (Al_2O_3, Fe_2O_3, CaO, *etc.*) and surface irregularities of silica matrix in CGS, selectively removing inorganic components and destabilizing their compact structural arrangement to generate hierarchical porosity. The H^+ ions progressively etch along contiguous metal oxide domains from the exterior to the interior surfaces, creating mesoporous networks.

Zhang *et al.*[52] prepared an adsorbent with a specific surface area of 393 $m^2\ g^{-1}$ and pore volume of 0.405 $cm^3\ g^{-1}$ using hydrochloric acid treatment (solid-to-liquid ratio 1 : 6, reacted at 600 °C for 3 h). Zhu *et al.*[53] elucidated the mesopore development mechanism under acid etching conditions, wherein H^+ ions progressively etched along contiguous metal oxide domains from exterior to interior surfaces, creating dendritic mesoporous networks, as shown in Fig. 3a. The original surface of CGS is very smooth, and the acid-etched CGS exhibits dendritic channels with diameters ranging from 2 to 6 nm. The TEM results in Fig. 3b provide evidence for analyzing the formation mechanism of the pores in CGS.[53] The resultant

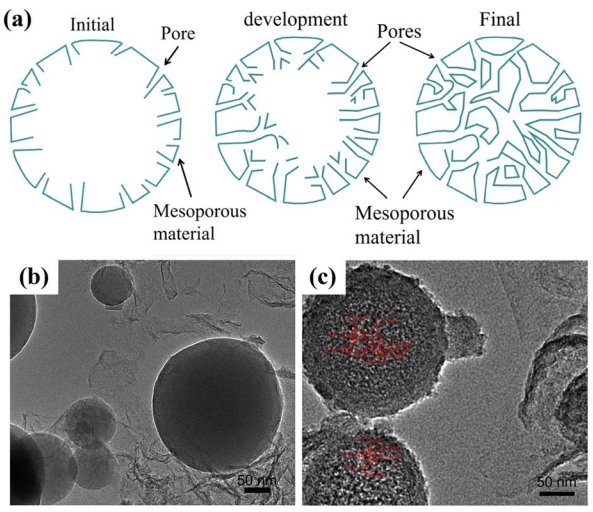

Fig. 3 (a) Evolution pathways of CGS-based mesoporous structures under acid etching. TEM image of (b) CGS and (c) CGS after acid etching. Reproduced with permission from ref. 53, copyright 2020, Elsevier.

carbon/silica composite exhibited a specific surface area of 337.51 $m^2 g^{-1}$ and pore volume of 0.341 $cm^3 g^{-1}$, substantiating the precise pore structure modulation capability of acid etching processes.[53]

Pore structure regulation is influenced by the carbon content and fine slag particle size. It has been observed that CGS carbon content modulates acid etching sites *via* redistribution of original mineral phases. Specifically, elevated CGS carbon content correlates with reduced inorganic content and increased initial specific surface area.[43] However, acid etching preferentially targets inorganic phases, resulting in constrained specific surface area enhancement for high-carbon materials. The physical obstruction caused by slag particles impedes micropore development, as Miao *et al.*[54] demonstrated that these particles occlude micropore channels within porous matrices.

Reasonably regulating acid type and concentration can synergistically optimize porosity and structural stability. Taking HCl as example, as strong acid, it has strong reactivity and can rapidly etch materials to prepare high-surface-area porous materials. Liu *et al.*[55] treated CGS with 16 wt% HCl and obtained carbon/silica composite porous material with specific surface area of 500 $m^2 g^{-1}$ and pore volume of 0.54 $cm^3 g^{-1}$. This demonstrates that process parameter adjustment in strong acid systems can achieve concurrent porosity enhancement and structural integrity. In contrast, HAc, as weak acid, reacts more gently, which helps to reduce the risk of over-etching and can be used for fine-tuning the pore structure. Du *et al.*[56] reported that increasing HAc concentration produced parabolic response in specific surface area, pore volume, and mesoporosity, with optimal performance achieved at 6 M HAc (specific surface area = 97.8 $m^2 g^{-1}$; pore volume = 0.206 $cm^3 g^{-1}$). However, it is noteworthy that while HCl demonstrates superior etching performance, it incurs higher acid consumption and wastewater treatment costs. Conversely, although HAc is environmentally friendly and reduces the risk of over-etching, its reaction rate is relatively slow. Therefore, in practical applications, the appropriate acid type should be selected based on a comprehensive consideration of etching speed, cost, and environmental impact, and the optimal etching time should be determined through experiments.

Acid etching methods offer operational simplicity and economic efficiency but are hindered by high acid consumption, waste management costs, and structural degradation from excessive etching. In the future, green processes such as acid solution recycling and bio-acid substitution can be used to mitigate environmental impacts. Additionally, template-assisted etching depth control could preserve structural stability while enhancing porosity. The method of combining process optimization with structural design may expand high-value applications and achieve dual improvements in environmental sustainability and material performance.

3.2 Alkali activation method

The alkali activation method constructs porous networks *via* multi-path reactions between strong bases (KOH, NaOH) and both the carbonaceous matrix and inorganic components of CGS.[57–59] Taking KOH as an example, its alkali activation mechanism primarily involves the following steps. Initially, redox reactions between KOH and carbonaceous matrix ($4KOH + C \rightarrow K_2CO_3 + K_2O + 2H_2\uparrow$) produce gaseous activating agents (CO_2/H_2O), which induce physical diffusion-mediated etching of carbon layers to create initial porosity. Subsequently, metallic K generated from the reaction intercalates into the carbon lattice, causing structural expansion during washing and removal processes that generate permanent pores. Ultimately, gasification reactions between H_2O/CO_2 and the carbon matrix further develop the porous architecture.[60]

Activation time and temperature play crucial roles in the pore-formation process. You *et al.*[58] utilized KOH to activate CGS for the preparation of activated coke. The experimental results demonstrated that an activation temperature of 850 °C and an activation time of 45 min represented the optimal conditions, under which the obtained activated coke exhibited the best adsorption performance for methyl orange. The yield of activated coke based on CGS first increased and then decreased with the prolongation of activation time. This phenomenon can be attributed to the ablation of carbon atoms during the activation process. When the activation temperature was below 850 °C, an increase in temperature intensified the reaction between KOH and residual carbon, leading to an enhanced yield. However, when the temperature exceeded 900 °C, substantial pyrolysis of the residual carbon occurred, resulting in a sharp decline in the yield.

In reducing atmospheres, metal oxides (Fe_2O_3, Al_2O_3) in CGS undergo carbothermal reduction (*e.g.* $Fe_2O_3 + 3C \rightarrow 2Fe + 3CO\uparrow$). The surface-reduced metal nanoparticles act as catalytic sites, lowering the energy barrier for KOH-carbon reactions and accelerating activation rates.[61] Xu *et al.*[62] demonstrated that Fe-active site construction on CGS surfaces *via* this synergy enhances catalytic pyrolysis and pore formation. Miao *et al.*[61] achieved 1187 $m^2 g^{-1}$ specific surface area and 0.89 $cm^3 g^{-1}$ pore volume using KOH activation, elucidating the transformation process of metal oxides during the KOH activation process, as shown in Fig. 4. The impregnation stage employs solid–liquid diffusion to infiltrate KOH solutions while dissolving metallic species for uniform dispersion across the carbon matrix. During subsequent heating and isothermal treatment, dissolved metals catalyze carbon skeleton pyrolysis and weaken structural bonds through direct carbon matrix interactions, synergistically improving physical activation efficiency.

While alkali activation offers low-temperature efficiency and tunable porosity, challenges persist regarding purification costs and equipment corrosion. Future directions include substituting pure alkalis with industrial waste liquids (*e.g.*, red mud leachate) to reduce costs and implement waste-to-waste solutions. Additionally, integrating external field-assisted heating could shorten reaction times and reduce equipment exposure to corrosive agents.

3.3 Physical activation method

Physical activation uses activators (air, CO_2, or steam) to interact with carbonaceous materials at high temperatures

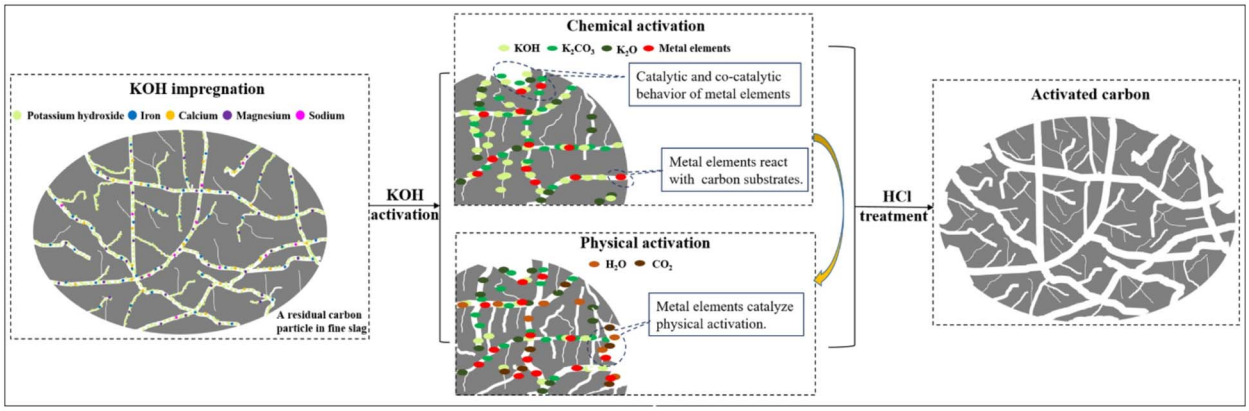

Fig. 4 Evolution pathways of CGS-based mesoporous structures under alkali activation. Reproduced with permission from ref. 61, copyright 2021, Elsevier.

(800–1100 °C), thereby promoting the development of pore networks in porous materials. During this process, the high-temperature decomposition of organics generates volatile species (CH_4, CO, *etc.*), the exudation of which creates initial porosity. Subsequently, activator molecules selectively oxidize defective edge-carbon atoms, promoting pore enlargement through oxidative erosion.[63]

The prior gasification processing of RC results in substantial volatile depletion and graphitic ordering, significantly reducing physical activation efficiency. Kang *et al.*[64] demonstrated CO_2-activated CGS achieving 862.76 $m^2\ g^{-1}$ specific surface area and 0.684 $cm^3\ g^{-1}$ pore volume, yet mesopore contribution remained limited (24.4% of total volume), indicating predominant micropore development. To enhance activation efficacy, calcium-based additives were incorporated to catalyze gas–carbon reactions. Zhang *et al.*[65] reported that $CaCO_3$ promotes the carbon–steam reaction ($C + H_2O \rightarrow CO + H_2$) during steam activation, with surface-bound Ca^{2+} ions acting as catalytic sites to reduce activation energy and accelerate lattice etching. The optimized formulation containing 8 wt% $CaCO_3$ yielded microporous carbon with 564 $m^2\ g^{-1}$ surface area and 0.24 $cm^3\ g^{-1}$ pore volume, accompanied by enhanced π–π* electronic transitions, surface alkaline functional groups were exposed, improving adsorption performance.

While physical activation offers mild operating conditions, low equipment corrosion, and clean exhaust, its energy intensity remains a concern due to high-temperature requirements. Additionally, inherent Al_2O_3/SiO_2 inorganic particles in CGS tend to occlude pore networks, particularly in coarse slags with prolonged gasifier residence times. Fine slags exhibit greater suitability owing to their higher carbon content and lower ash fractions. Future advancements should focus on pretreatment strategies such as size fractionation and acid leaching to purify RC feedstocks, potentially integrating chemical activation methods to overcome pore development limitations.

3.4 Hierarchical synthesis method

The hierarchical synthesis method integrates the merits of acid etching, alkali activation, and physical activation to enhance CGS utilization efficiency.[7,66,67] Incorporation of templating agents enables precise regulation of pore architectures, offering novel pathways for fabricating carbon/silica and carbon/molecular sieve composite porous materials. Alkali treatment activates metallic compounds within CGS, accelerating acid-reaction kinetics and leaching efficacy. This property allows acid-base sequential processing to enrich RC porosity and intensify CGS etching efficiency, yielding carbon/silica composites with advanced pore development. For instance, Gu *et al.*[68] achieved 1347 $m^2\ g^{-1}$ specific surface area and 0.69 $cm^3\ g^{-1}$ total pore volume *via* KOH activation coupled with acid washing. Hydrochloric acid concentration significantly influences porous material surface area, with acid-leached SiO_2 fragments templating mesopore formation through aligned carbon micropores. The reaction mechanism during the preparation process and the TEM images of the material before and after the reaction are shown in Fig. 5. Miao *et al.*[69] obtained CGS-based porous materials exhibiting 2194 $m^2\ g^{-1}$ surface area and 2.095 $cm^3\ g^{-1}$ pore volume after hierarchical synthesis and hydrothermal treatment. Liu *et al.*[70] developed hierarchical activated carbon/mesoporous silica microspheres from CGFS through graded methodology, achieving 625.45 $m^2\ g^{-1}$ surface area and enhanced MB adsorption performance.

The acid-base synergy within hierarchical synthesis facilitates the creation of interconnected micropore–mesopore–macropore architectures, offering highly customizable pore designs. This approach enables precise control over pore structure, thereby enhancing the material's specific surface area and pore volume. However, the multi-step nature of this process poses significant challenges, including elevated energy consumption, the generation of acid-base waste, and inadequate pore stability, which can compromise the material's long-term performance. Future advancements may include developing one-step simplified processes, exploring green activators like ionic liquids, and implementing molecular simulations for pore design optimization to drive application innovations in emerging domains.

3.5 Comparative analysis of preparation methods

The preparation methods for CGS-based porous materials are exhibiting a diversified development trend, with each method

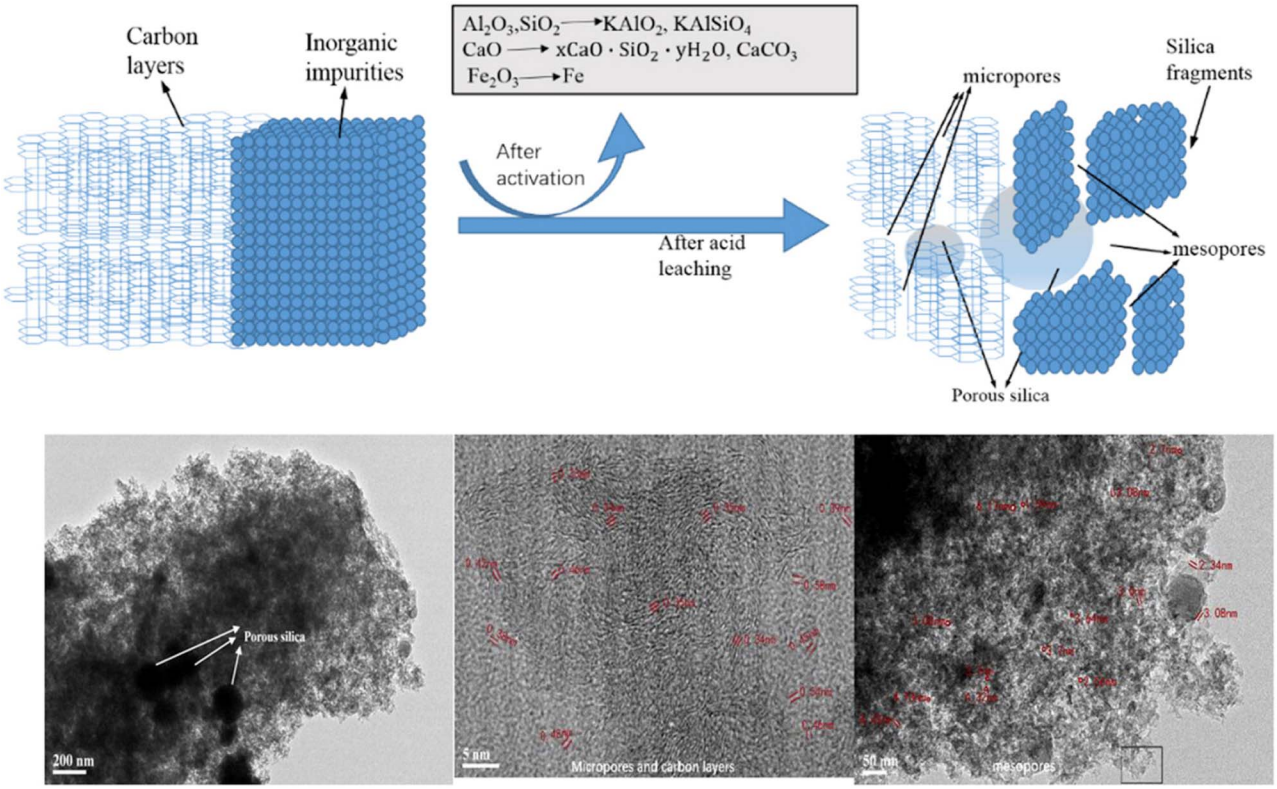

Fig. 5 Reaction mechanism and TEM images of porous material before and after preparation. Reproduced with permission from ref. 68, copyright 2019, Elsevier.

possessing unique application scenarios and performance characteristics. To ensure that the pore structure of the prepared materials exhibits good reproducibility and stability, thereby meeting various specific application requirements, it is necessary to optimize the preparation processes and regulate the process parameters for different activation methods or

Table 2 Preparation method and pore structure characteristics of CGS-based porous materials

Synthetic method	Material	S ($m^2\ g^{-1}$)	V ($cm^3\ g^{-1}$)	Pore size (nm)	Ref.
HCl etching	Resin adsorbent	393	0.405	4.739	52
HCl etching	Carbon/silicon composite mesoporous material	334.40	0.328	5.394	53
HAc etching	Mesoporous material	500	0.54	2–5	56
HCl etching	Carbon/silicon composite mesoporous material	97.8	0.206	2–10	55
KOH activation	Activated carbon	1464.39	0.59	2.57	57
KOH activation	Activated coke	422.16	0.30	2.86	58
KOH and NaOH activation	Porous carbon	1052.78	0.66	2.75	59
KOH activation	Activated carbon	1187	0.89	3.50	61
NaOH activation	ZSM-11 zeolite	100.69	0.235	9.32	62
CO_2 physical activation	Activated carbon	1203	0.509	—	63
CO_2 physical activation	Activated carbon	862.76	0.684	2.45	64
Steam activation	Activated carbon	671	0.31	1.62	65
KOH activation and HCl etching	Carbon/silicon composite mesoporous material	1275.63	0.26	2.2	66
NaOH activation + HCl etching	Carbon/silicon composite mesoporous material	8.0	0.01	5.5	67
KOH activation + HCl etching	Carbon/silicon composite mesoporous material	1347	0.69	3.44	68
KOH activation + HNO_3 etching	Carbon/silicon composite mesoporous material	2194	2.095	3.82	69

etching techniques. Table 2 illustrates the preparation methods and pore structure characteristics of CGS-based porous materials, providing a basis for the selection of preparation methods and the adjustment of process parameters.

Acid etching method is suitable for CGS systems with high inorganic content, and its selective dissolution characteristics can efficiently remove ash content, but it requires high equipment corrosion resistance. Alkali activation is optimized for carbon-rich CGS feedstocks, utilizing intense alkaline environments to disrupt carbonaceous structures, though challenges persist in alkali solution recyclability. Physical activation suits large-scale processing of RC-rich CGS, offering clean operational advantages but pore development constraints related to precursor graphitization levels. Hierarchical synthesis addresses systems with balanced inorganic/RC composition, employing acid-base synergies and template-guided engineering to achieve graded pore architectures with tailored functionality, yielding materials exhibiting dual microporous adsorption and mesoporous transport capabilities. To further compare and analyze the four CGS-based porous material preparation methods, Table 3 presents their differences in terms of pore formation mechanisms, advantages and disadvantages, scalability, regulatory challenges, as well as environmental and economic considerations.

From the perspective of pore structure size, hierarchical synthesis method > alkali activation method > physical activation method > acid etching method. The hierarchical synthesis method yields pores with the largest specific surface area. Moreover, it enables the gradient design of pore structures and the customization of functionalities. However, the complexity of its process flow leads to an increase in both process costs and time.

The physical activation method demonstrates relatively good pore-forming performance. Its preparation process is environmentally friendly, with minimal wear on equipment. Nevertheless, this method suffers from high energy consumption and cost. Moreover, when dealing with CGS materials with complex structures or fine particle sizes, it is prone to pore-channel blockage. The acid etching and alkali activation methods are characterized by simple processes and high pore-forming efficiency. However, they also bring about issues such as high purification costs and severe equipment corrosion. Additionally, compared with the hierarchical synthesis method, the porous materials produced by these two methods exhibit certain deficiencies in terms of pore uniformity, specific surface area, or functional groups. Considering factors such as efficiency, cost, and customization requirements, if the process of the hierarchical synthesis method can be optimized and the cost reduced, it may be an ideal approach for preparing high-quality CGS-based porous materials.

The selection of material preparation methods should comprehensively consider the composition of raw materials,

Table 3 Comparison of preparation methods for CGS-based porous materials

Method	Acid etching	Alkali activation	Physical activation	Hierarchical synthesis
Mechanism	Reaction of strong acid with metal oxides to form hierarchical pores	Reaction of strong alkali with carbon matrix and aluminosilicates to construct a three-dimensional pore network	Pyrolysis pore formation using activators such as CO_2/steam at high temperatures	Multi-scale coupled activation process to achieve precise control of pore structure
Advantage	Simple process, low cost, high pore development efficiency	Efficient at low temperatures, strong controllability of pore structure	Clean and environmentally friendly, low equipment wear and tear	Excellent comprehensive performance, controllable pore gradient
Disadvantage	High acid consumption, high cost of waste liquid treatment	High purification cost, severe equipment corrosion	High energy consumption, inorganic particles easily block pores	Complex process, higher cost
Object	CGS with high inorganic content	CGS with high carbon content	CGS with high carbon content	CGS with similar contents of inorganic matter and residual carbon
Scalability	Limited scalability due to high acid consumption and waste treatment challenges	Moderate scalability, but equipment corrosion may limit long-term operation	Scalable but energy-intensive, requiring significant energy resources	Limited scalability due to process complexity and high cost
Regulatory challenges	Stringent environmental regulations on acid waste disposal	Strict regulations on alkali use and waste disposal to prevent environmental contamination	Compliance with energy efficiency and emissions regulations	Stringent regulations on process safety and waste management
Environmental and economic considerations	High environmental impact due to acid waste; economic feasibility depends on waste treatment costs	Equipment corrosion increases maintenance costs; environmental concerns regarding alkali waste	Energy-intensive process; potential for pore blocking may affect product quality and yield	High process complexity increases costs; may require specialized equipment and expertise

the desired pore structure, and specific application requirements. To facilitate the practical application of these methods, it is essential to establish a correlation model linking "composition-process-performance." Comprehensive characterization of the mineral composition and carbon structural characteristics of CGS using techniques such as XRF and XRD is necessary. By matching process parameters with raw material properties, the customization and functionalization of CGS-based porous materials can be promoted, optimizing their performance for specific applications.

4. Applications of CGS-based porous materials

CGS-based porous materials offer significant potential for applications in heavy metal ion adsorption,[71–73] organic pollutant removel,[74–76] CO_2 capture,[77,78] polymer reinforcement,[79–81] and electromagnetic wave absorption.[82,83]

4.1 Heavy metal ion adsorption

Heavy metal contaminants including cadmium, copper, nickel, and lead present substantial risks to both ecosystems and human health. Porous adsorbents have been engineered to enable selective heavy metal ion capture through tailored pore architectures and surface chemistries.[84] Porous carbon and mesoporous silica exhibit excellent adsorption performance for heavy metal ions due to its high specific surface area and tunable pore structure. Xu *et al.*[85] chemically activated CGS with KOH to obtain graded porous carbon, demonstrating an ultra-high specific surface area of 2481 $m^2\ g^{-1}$. The material demonstrated Pb^{2+} uptake capacity of 141 mg g^{-1}. Its adsorption kinetics following pseudo-second-order model and Freundlich isotherm. Acid-leached CGS-based mesoporous silicas produced by Yang *et al.*[86] achieved 99% Ga^{3+} removal efficiency. Fig. 6 presents the results of investigating Ga(III) adsorption on HCl-CGS through EDS, FTIR, and XPS analyses. EDS images (Fig. 6a–d) display significant Ga signals after adsorption, confirming its presence on the surface; FTIR spectra (Fig. 6e) show intensified peaks at 3425 cm^{-1} (H_2O) and 1632 cm^{-1} (–OH) along with a new peak at 617 cm^{-1}, suggesting the adsorption of $Ga(OH)_4^-$ and the formation of O–Ga bonds; XPS analysis (Fig. 6f) reveals Ga3p1 and Ga2p3 peaks post-adsorption, indicating Ga(III) coordination with the adsorbent, while the O 1s spectra (Fig. 6g and h) display an increased O–H signal and an O–Ga peak at 530.9 eV, further supporting the

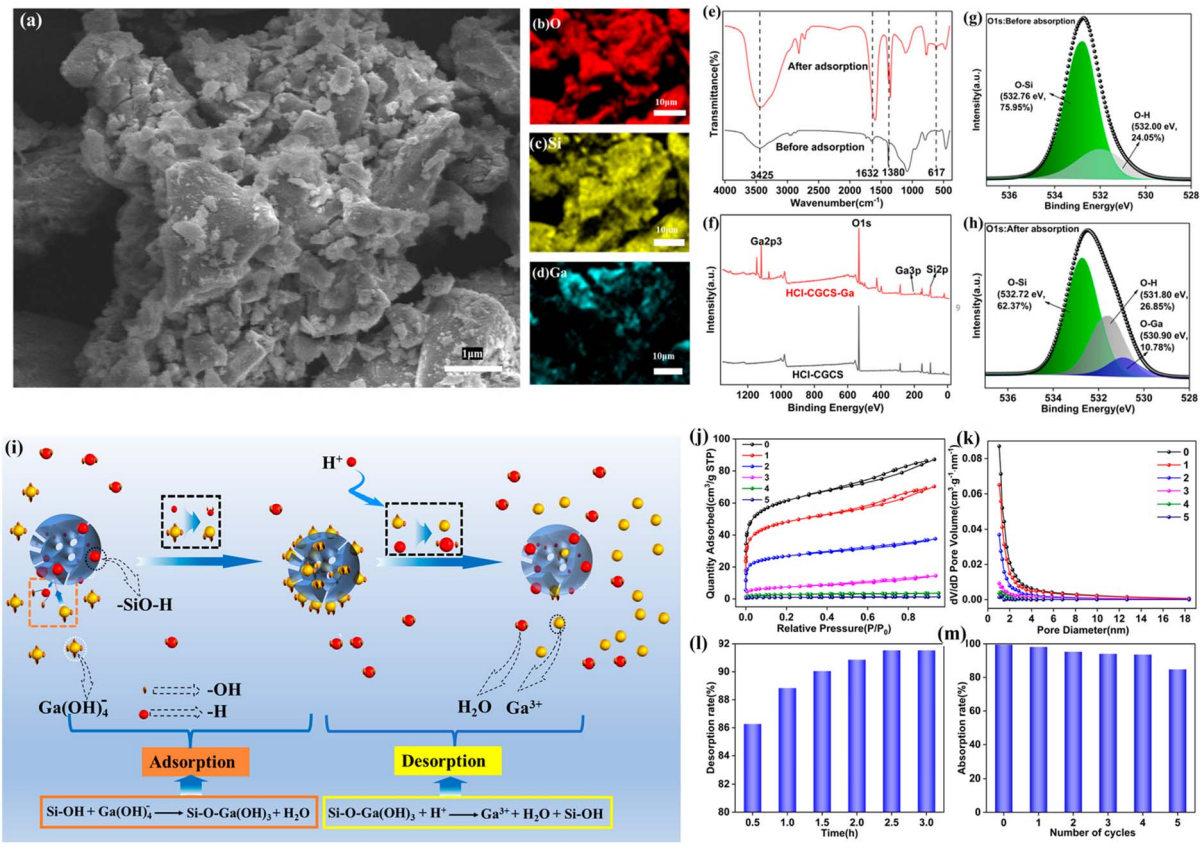

Fig. 6 (a) SEM images of HCl-CGCS after Ga(III) adsorption. Elemental distribution EDS maps of (b) O, (c) Si, and (d) Ga. (e) FTIR spectra before and after Ga adsorption. (f) XPS survey spectrum. O 1s fine spectrum of HCl-CGCS (g) before Ga adsorption and (h) after Ga adsorption. (i)The adsorption and desorption principle of Ga^{3+} on CGS-based mesoporous silicas mesoporous silica surface. (j) Adsorption–desorption isotherms of HCl-CGCS after 5 cycles. (k) Pore size distribution. (l) Effect of HCl solution elution time on desorption efficiency. (m) Adsorption performance after 5 cycles. Reproduced with permission from ref. 86, copyright 2024, Multidisciplinary Digital Publishing Institute.

formation of O–Ga bonds through electrostatic and chemical interactions. After adsorption, a significant Ga signal was observed on HCl-CGCS, confirming the effective adsorption of Ga(III) on the material surface (Fig. 6i). Furthermore, the material maintained an adsorption efficiency of > 85% after undergoing five cycles of regeneration, as shown in Fig. 6j–m.

In contrast, zeolitic composites shift the adsorption mechanisms toward chemisorption. The adsorbate is chemically bound to the adsorbent, often resulting in stronger adsorption and potentially more selective removal of specific ions. Alkali-fused slag-based Na-zeolites developed by Lv *et al.*[87] exhibited 16.49 mg g^{-1} Pb^{2+} adsorption with 82.45% removal, monolayer chemisorption confirmed by recyclability tests involving electrostatic interactions and ion exchange. However, differences exist in the adsorption processes of various heavy metal ions. Cui *et al.*[88] fabricated magnetic zeolite A composites *via* red mud/CGS synergy, achieving 330.72 mg g^{-1} Pb^{2+} and 142.72 mg g^{-1} Cu^{2+} adsorption. Langmuir monolayer behavior governed Pb^{2+} capture while Cu^{2+} followed Freundlich multilayer kinetics, highlighting metal-specific adsorption mechanisms.

4.2 Organic pollutant removal

CGS-based porous materials not only demonstrate the capability to adsorb heavy metal ions but also exhibit significant organic pollutant capture abilities.[70,89–92] Niu *et al.*[89] transformed CGS into three-dimensionally interlaced porous carbon/mineral composite electrodes using hierarchical synthesis methodology. Compared with conventional planar electrodes, the degradation rate of *m*-Cresol by the three-dimensional composite electrode was significantly enhanced by 2.6 times (reaching 79.61 mg L^{-1}). Traditional planar electrodes typically exhibit limited surface area and mass transfer efficiency, which constrains their pollutant degradation capabilities. In contrast, the three-dimensional structure of the composite electrode based on CGS offers a larger surface area for electrochemical reactions and facilitates improved mass transfer of reactants and products, enabling the complete purification of *m*-Cresol within 24 min. The enhancement in electrocatalytic efficiency can lead to a more efficient and cost-effective wastewater treatment process, reducing both the time and energy required for pollutant removal. Through hierarchical synthesis strategies, Liu *et al.*[70] fabricated tiered activated carbon (TAC) and amino functionalized mesoporous silica microspheres (AMSM). The adsorption capacity of TAC for methylene blue was found to be 1708.01 mg g^{-1}, while that of AMSM was 1249.46 mg g^{-1}. In comparison with traditional carbon materials and other porous adsorbents, TAC exhibits advantages due to its multi-layer retention mechanism, which combines pore filling, hydrogen bonding, electrostatic interactions, and π–π stacking. On the other hand, AMSM primarily utilizes electrostatic attraction and hydrogen bonding, also demonstrating favorable adsorption performance. In contrast, traditional carbon materials and porous adsorbents predominantly rely on simple pore-filling mechanism, which limits their adsorption capacity and selectivity.

Building upon these advances, Long *et al.*[91] extended CGS applications by synthesizing Fe–C composites *via* peroxymonosulfate (PMS) activation. The defective carbon matrix in CGS facilitates electron transfer while Fe species and oxygen-containing functional groups synergistically catalyze reactive oxygen species generation at the solid–liquid interface, enabling oxidative–adsorptive sulfamethoxazole (SMX) removal with significantly enhanced efficiency. As illustrated in Fig. 7, a proposed mechanism for SMX degradation in the CGS-1000/PMS system involves PMS activation primarily by surface-bound radicals, singlet oxygen ($^1O_2$), and direct electron transfer. Initially, $SO_4^{\cdot-}$ and ·OH radicals are generated through the traditional Fe-mediated PMS activation process, while the sp^2 hybridized carbon matrix edge and C–OH groups also contribute to radical generation by donating π electrons to

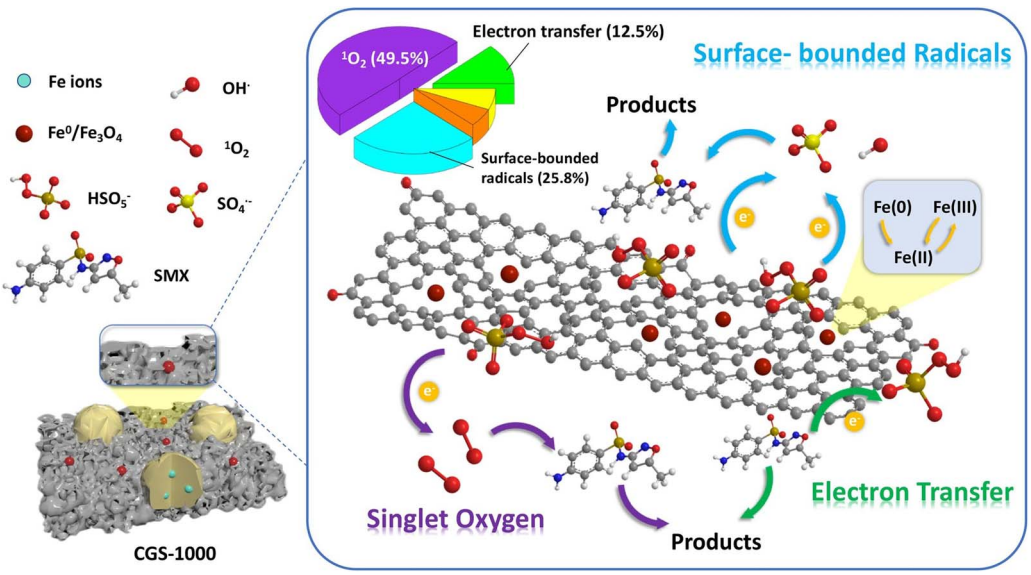

Fig. 7 Mechanism of SMX degradation in the Fe–C composites. Reproduced with permission from ref. 91, copyright 2023, Elsevier.

PMS. These radicals preferentially attach to the electron-rich carbon matrix surface, becoming surface-bound. Secondly, $^1O_2$ plays a more prominent role in SMX degradation than $SO_4^{-}\cdot$ and ·OH, mainly produced *via* PMS accumulation on the carbon electron system with subsequent self-decomposition and through nucleophilic addition at ketonic carbonyl (C═O) groups on the carbon structure. Finally, direct electron transfer between PMS and SMX occurs on the sp^2 hybridized carbon matrix surface, leading to the direct decomposition of SMX without reactive oxygen species involvement. Conventional materials employed for analogous pollutant removal are generally unable to simultaneously execute adsorption and oxidation processes. And they may exhibit relatively low catalytic activity, which consequently leads to diminished removal efficiencies. Notably, CGS-based materials also exhibit quantifiable adsorption capacities toward inorganic contaminants such as phosphate (PO_4^{3-}) and ammonium (NH_4^{+}).[53,93,94]

4.3 CO_2 capture

Within the Carbon Capture, Utilization and Storage (CCUS) technology framework, CGS-based porous materials are realizing improvements in CO_2 adsorption performance *via* process innovations.[59] Leveraging their inherent pore characteristics and compositional advantages in ash residues, a series of cost-effective, high-performance adsorbent fabrication strategies have been developed.[61,95–98] Wei *et al.*[99] synthesized hierarchical porous nanostructured silica *via* acid leaching-alkali dissolution-assisted hydrothermal processes. The resulting material possessed a specific surface area of 457 $m^2\ g^{-1}$ and pore volume of 2.34 $cm^3\ g^{-1}$, achieving adsorption capacities of 2.87 mmol g^{-1} (20 °C) and 8.49 mmol g^{-1} (15% CO_2). The Si–O–Na/Al network formed through aluminosilicate self-assembly augmented porosity and enhanced adsorption activity *via* abundant silanol groups (Fig. 8). Equilibrium was reached within 10 min, with no performance degradation observed after 20 cycles. Adsorption behavior alignment with the Sips model further confirmed the material's stable and reliable performance characteristics. Miao *et al.*[54,69] prepared CCGS-based porous carbon material with specific surface area of 1295 $m^2\ g^{-1}$ *via* alkali activation method. At 25 °C, this material achieved CO_2 adsorption capacity of 2.64 mmol g^{-1} and reached adsorption equilibrium within 2 min. Furthermore, the research team conducted HNO_3 etching on the alkali-activated porous material. The etched sample exhibited an increased specific surface area of 2194 $m^2\ g^{-1}$, accompanied by a corresponding rise in CO_2 adsorption capacity to 5.32 mmol g^{-1}.

In addition, the introduction of highly reactive carboxyl (–COOH) functional groups through amine modification can improve the surface properties of materials and enhance their CO_2 adsorption capabilities. Zhang *et al.*[97] fabricated a mesoporous fine slag adsorbent (FSA) material with a specific surface area of 541 $m^2\ g^{-1}$ and a pore volume of 0.543 $cm^3\ g^{-1}$ using CGS as the raw material. Amine-functionalized adsorbents were prepared by physically impregnating tetraethylenepentamine (TEPA) onto the FSA material. The adsorbent achieved CO_2 adsorption capacity of 132.5 mg g^{-1}. The good dispersibility of TEPA molecules within the CGS pores effectively prevented agglomeration, improved the accessibility of active sites, and facilitated the suppression of amine leaching. Meanwhile, the small steric hindrance and high affinity of TEPA for CO_2 reduced mass transfer resistance, further enhancing the adsorption performance. Moreover, the cost of this amine-functionalized adsorbent is significantly lower than that of other mesoporous materials, suggesting its advantages and potential for industrial production and large-scale applications. Employing CGFS as precursor, Table 4 outlines recent advances in adsorption applications of CGS-based porous materials.

4.4 Polymer composite reinforcement

CGS materials demonstrate distinct advantages in polymer modification applications due to their unique globular morphology. This is fundamentally different from the angular geometry of traditional inorganic fillers (*e.g.*, $CaCO_3$). The spherical geometry of CGS particles reduces stress concentration at particle–matrix interfaces, enabling superior load transfer efficiency compared to sharp-edged fillers. The non-destructive nature of their molecular chain interactions and superior dispersibility render them viable alternatives to conventional inorganic fillers.[52] Through acid etching, Zhang *et al.*[79] fabricated hierarchical porous CGS fillers with a specific surface area of 564 $m^2\ g^{-1}$ and pore volume of 0.807 $cm^3\ g^{-1}$. Incorporation of these fillers at 30 wt% loading resulted in a 67.6% reduction in volatile organic compounds (VOCs) emissions from polypropylene (PP) composites. The preparation process and performance improvement are shown in Fig. 9. Chemical anchoring mechanisms were identified as the primary contributor to enhanced interfacial bonding, with measured increases in tensile strength (49.84%), impact strength (70.81%), and flexural strength (139.63%) compared to traditional $CaCO_3$-based systems. The spherical morphology of CGS particles minimizes stress concentration at the particle–matrix interface, thereby reducing interfacial defects. In contrast, angular $CaCO_3$ particles are tend to initiating crack propagation. This performance disparity underscores the

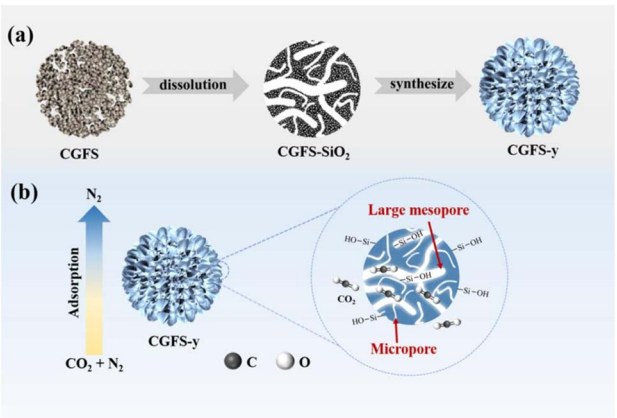

Fig. 8 Hierarchical porous silica nanoparticles (a) formation process. (b) Adsorption process. Reproduced with permission from ref. 99, copyright 2025, Elsevier.

Table 4 Pore structure characteristics and adsorption performance of CGS-based porous materials in adsorption

Material	Surface area ($m^2\ g^{-1}$)	Pore volume ($cm^3\ g^{-1}$)	Pore size (nm)	Adsorbate	Adsorbate capacity	Ref.
Nanoporous glass microspheres	4.554	0.014	5.627	Pb^{2+}	302.39 mg g^{-1}	84
Porous carbon	2481	1.711	1.2–4	Pb^{2+}	141 mg g^{-1}	85
Mesoporous silica	258.4	0.152	2.363	Ga^{3+}	3.96 mg g^{-1}	86
Magnetic A-type zeolite	35.17	0.041	5.76	Pb^{2+}	330.72 mg g^{-1}	88
Magnetic A-type zeolite	35.17	0.041	5.76	Cu^{2+}	142.72 mg g^{-1}	88
Nanoporous glass microspheres	4.554	0.014	5.627	Congo red	342.74 mg g^{-1}	84
Hierarchical activated carbon	648.82	0.462	5.491	Methylene blue	1708.01 mg g^{-1}	70
Mesoporous silica microspheres	176.28	0.161	5.657	Methylene blue	1249.46 mg g^{-1}	70
Magnetic carbon–silicon composite	196.84	0.346	3.20	Rhodamine B	188.68 mg g^{-1}	92
Mesoporous silica microspheres	541	0.543	3–4	CO_2	132.5 mg g^{-1}	97
Hierarchical porous materials	1405	0.19	0.4–3.8	CO_2	4.06 mol kg^{-1}	98
Hierarchical nano-silica materials	457	2.34	20.46	CO_2	2.87 mmol g^{-1}	99
Hierarchical porous composites	1295	0.92	19.24	CO_2	2.64 mmol g^{-1}	54
Porous composite materials	2194	2.095	3.82	CO_2	5.32 mmol g^{-1}	69

potential for CGS to supplant conventional fillers. Employing acid dissolution and temperature-programmed calcination, Ai *et al.*[80,81] developed mesoporous spherical silica/porous carbon composite fillers. Synergistic interactions between mesoporous SiO_2 and amorphous carbon components were observed to significantly elevate tensile strength while enhancing interfacial compatibility, thereby enabling complete substitution of heavy calcium carbonate in PP composites. Subsequent investigations revealed that in ABS systems, the spherical morphology of CGS particles, as opposed to the angular geometry of $CaCO_3$, improved interfacial adhesion by 40%. This structural advantage optimizes material flowability while reducing processing energy consumption. The resultant balance of rigidity and toughness introduces innovative material solutions for engineering plastics and functional films, particularly in precision component manufacturing where high impact resistance and minimal warpage deformation are critical.

4.5 Electromagnetic wave absorption

CGS exhibits synergistic interactions between graphitized carbon and oxygen-containing functional groups, enhancing composite dielectric properties.[100,101] In the field of electromagnetic wave absorption, "minimum reflection loss (RL)" and "effective absorption bandwidth (EAB)" are recognized as pivotal indicators for evaluating the absorption performance of materials. RL reflects the capability of a material to suppress the reflection of electromagnetic waves; a smaller RL value signifies less reflection and stronger absorption. EAB denotes the

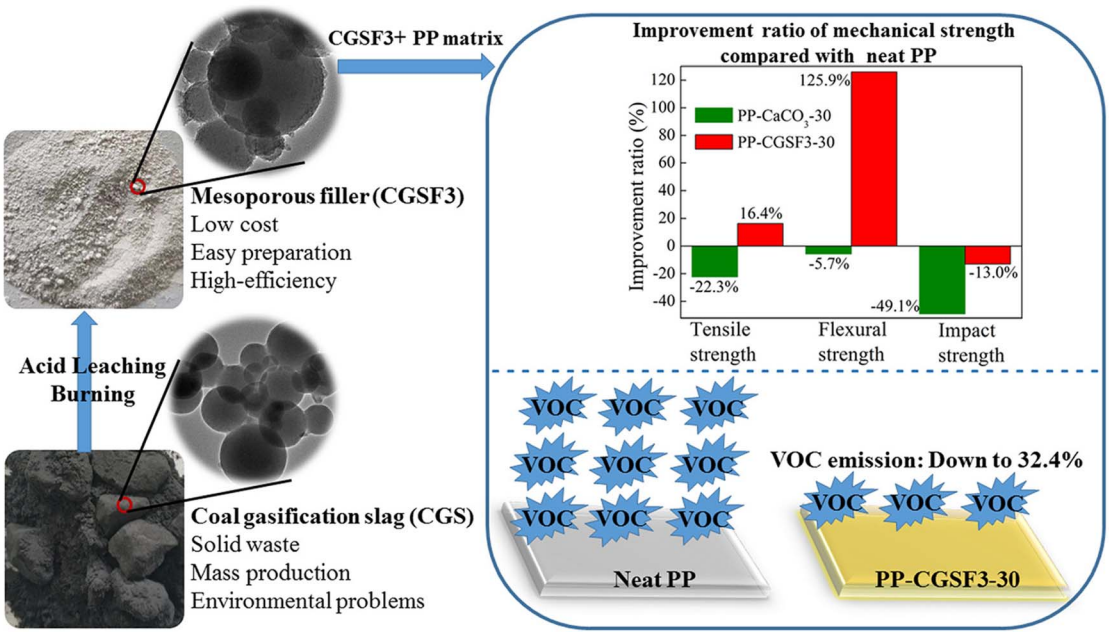

Fig. 9 Preparation process and performance enhancement of hierarchical porous CGS fillers. Reproduced with permission from ref. 79, copyright 2021, Elsevier.

frequency range over which a material can effectively absorb electromagnetic waves, with a broader range indicating greater adaptability to electromagnetic waves of varying frequencies. Gao *et al.*[102] incorporated $ZnSnO_3$ and refined fly ash to engineer ZSFA composites with multi-polarization mechanisms. The synthesized ZSFA exhibits remarkable maximum RL value of −47.8 dB at thickness of 2.5 mm, underscoring its enhanced dielectric loss capability (Fig. 10a and b). Additionally, it boasts the broadest EAB (RL ≤ −10 dB), spanning 7.0 GHz from 11.0 to 18.0 GHz. Notably, at a reduced thickness of just 2.2 mm, the EAB fully encompasses the entire Ku-band, as illustrated in Fig. 10c. This exceptional performance is attributable to its tailored conductive network and interfacial structures enabling tunable dielectric loss behavior. Fig. 10d–h elucidates the loss mechanisms, wherein enhanced polarization relaxation and electron mobility contribute to elevated microwave attenuation efficiency. Under the action of electromagnetic field, the positive and negative charges in $ZnSnO_3$ and at its interfaces deviate from their geometric centers, resulting in enhanced interfacial polarization. Meanwhile, the graphitized carbon facilitates polarization, thereby dissipating the incident microwave energy. After acid treatment, fly ash develops volumetric defects, causing the charged electrons to deviate from their equilibrium positions and leading to dipole polarization. CGS contains a graphitized carbon layer, which forms a unique conductive pathway, enabling rapid ballistic motion of electrons in the carbon substrate.

Given the inadequate impedance matching of single-carbon components, which limits their absorptive efficacy, dielectric and magnetic materials were integrated to produce magnetic-dielectric composites exhibiting robust absorption capacity and broadband performance at reduced thicknesses. Zhang *et al.*[82] achieved radar stealth capabilities with Cu_9S_5/CGFS composites through one-step hydrothermal synthesis, yielding a minimum RL of −25.01 dB with EAB spanning 3.52 GHz. This indicates that the Cu_9S_5/CGFS composite material exhibits a strong electromagnetic wave absorption capacity within specific frequency bands. Zhang *et al.*[83] prepared the $CoFe_2O_4$/CGFS composites material utilizing the graphitized framework of CGFS demonstrated exceptional magnetodielectric synergistic effects. At 7.76 GHz, the composite achieves RL of −43.99 dB with a thickness of 2.44 mm. The interaction between magnetic and dielectric materials further enhances the material's ability to dissipate electromagnetic waves. He *et al.*[103] developed Fe_3O_4@N-doped RC composite *via* N doping and Fe_3O_4 incorporation, augmenting dielectric and magnetic losses while optimizing impedance matching. This composite achieved an extreme RL of −41.4 dB at 1.5 mm thickness, with EAB of 4.32 GHz (13.68–18 GHz), surpassing conventional thickness-dependent absorbers. When compared with the

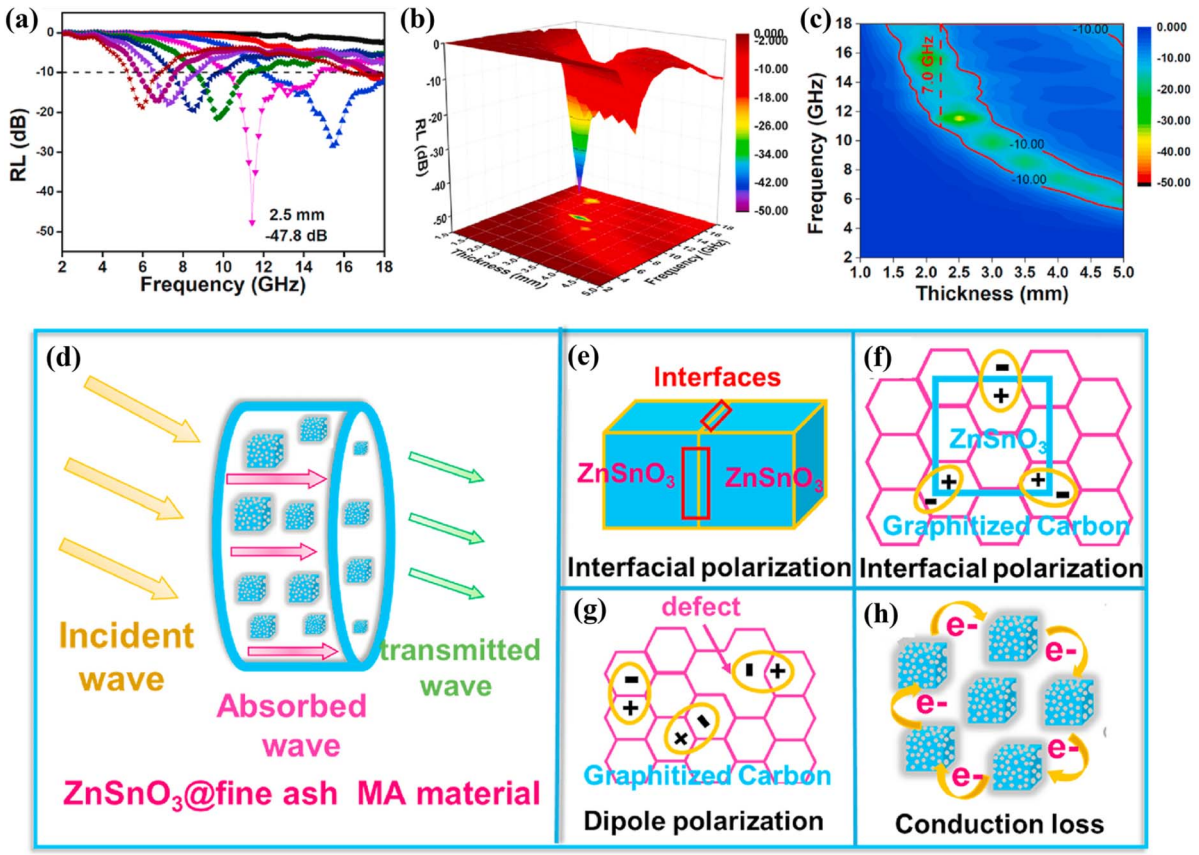

Fig. 10 (a) The reflection loss curve. (b) 3D reflection loss projection image. (c) Effective bandwidth. (d–h) Dielectric loss mechanism in ZSFA composite materials. Reproduced with permission from ref. 102, copyright 2021, Elsevier.

Table 5 Synthesis technology and high-value applications of CGS-based porous materials in recent years

Material	Synthetic method	Application	Performance	Reaction mechanism	Ref.
Porous carbon	Alkali activation	Adsorption of Pb^{2+}	Adsorption capacity up to 141 mg g^{-1}	Freundlich isotherm model and pseudo-second-order kinetics equation	85
Mesoporous silica	Acid etching	Adsorption of Ga^{3+}	At pH 9, removal efficiency of 99%	Pseudo-second-order kinetics and Langmuir model	86
Magnetic A-type zeolite	Alkali activation	Adsorption of Pb^{2+}, Cu^{2+}	At pH 4–5, adsorption capacities of 330.72 mg g^{-1} and 142.72 mg g^{-1} respectively	Langmuir monolayer model and Freundlich multilayer adsorption respectively	88
Porous carbon/mineral composite electrode	Alkali fusion-polymerization-hydrothermal	Degradation of *m*-Cresol	100% degradation rate within 24 h	Electro-adsorption of reactive oxygen species, physical adsorption, electrochemical oxidation catalysis	89
Hierarchical activated carbon and mesoporous silica microspheres	Hierarchical synthesis	Adsorption of methylene blue	Adsorption capacities of 1708.01 mg g^{-1} and 1249.46 mg g^{-1} respectively	Langmuir and Freundlich adsorption isotherm models and pseudo-second-order kinetics equation	70
Fe–C composite material	Alkali activation	Degradation of sulfamethoxazole	91.1% degradation rate within 90 min	Type IV isotherm model	91
Hierarchical porous materials	Chemical activation and hydrothermal synthesis	Adsorption of CO_2	Adsorption capacity of 4.06 mol kg^{-1}	Type IV isotherm model	98
Porous composite materials	Acid etching	Adsorption of CO_2	Adsorption capacity of 5.32 mmol g^{-1}	Type I/IV isotherm models	69
Hierarchical porous nano-silica materials	Acid leaching-alkali dissolution assisted hydrothermal	Adsorption of CO_2	Adsorption capacities of 2.87 and 8.49 mmol g^{-1} at 20 °C and 15% CO_2 concentration respectively	Pseudo-first-order kinetics model, pseudo-second-order kinetics model, and Avrami model	99
PP composite materials	Acid etching	Adsorption of VOCs	67.6% reduction in VOCs emissions	Type IV isotherm model	79
Mesoporous spherical silica/porous carbon composite filler	Acid dissolution and temperature-controlled calcination	Modification of tensile strength	Tensile strength increases initially and then decreases with decreasing carbon content	Turcsanyi model	80
Cu_9S_5/CGFS composite material	Hydrothermal synthesis	Microwave absorption	Reflection loss of −25.01 dB	Interfacial polarization and dipole polarization	82
$CoFe_2O_4$/CGFS composite material	Acid washing-hydrothermal synthesis	Microwave absorption	Reflection loss of −43.99 dB	Magnetodielectric synergistic effect	83
Fe_3O_4@N-Doped RC composite material	Chemical co-precipitation	Microwave absorption	Reflection loss of −41.4 dB	Magnetodielectric synergistic effect	103
ZSFA composite material	Alkali activation	Microwave absorption	Reflection loss of −47.8 dB	Strong polarization relaxation and electron migration capability	102

previous two materials, the Fe_3O_4@N-doped RC composite material achieves lower reflection loss and wider effective absorption bandwidth at thinner thickness, surpassing traditional absorbers that rely on thickness.

5. Conclusion and future direction

This paper reviews research progress on high-value applications of coal gasification slag (CGS)-based porous materials and analyzes their potential and challenges. Table 5 outlines recent advances in synthesis technologies and high-value applications of CGS-based porous materials. (1) As the major by-product of coal gasification, long-term CGS accumulation wastes land resources and poses ecological risks. However, its unique composition of RC and silicoaluminate minerals offers advantages for developing porous functional materials. Green conversion technologies enable the transformation of CGS from industrial waste into high-value materials. (2) CGS carbon content gradients allow tailored synthesis approaches: physical/alkali activation for high-carbon CGS, hierarchical synthesis for medium-carbon CGS, and acid etching for low-carbon CGS to remove minerals and create porosity. (3) Through compositional tailoring and process optimization, CGS-based porous materials show promise in environmental remediation, material reinforcement, and other fields, demonstrating the shift from waste to functional materials.

Despite their promising potential, CGS-based porous materials face several research and application challenges. Firstly, *in situ* characterization techniques, such as the combination of XRD and SEM-EDS, are required to elucidate activation-induced phase transformations and establish a robust framework for the "composition-structure–property" relationship. This will enable a deeper understanding of material behavior under different synthesis conditions. Secondly, the traditional alkali activation process generates a significant amount of alkaline wastewater, posing environmental concerns. To mitigate this issue, waste recycling strategies should be implemented, or more environmentally friendly activators such as ionic liquids should be adopted. Ionic liquids offer sustainable alternative due to their low volatility, high thermal stability, and tunable properties. Thirdly, it is crucial to enhance research on the long-term environmental durability and material stability of CGS-based porous materials. Accelerated aging tests and real-world exposure studies should be conducted to ensure performance reliability under operational conditions. This will provide valuable insights into material degradation mechanisms and inform the development of more durable materials. Finally, the current production costs of CGS-based porous materials remain high, hindering their commercial viability. To address this challenge, a comprehensive life-cycle economic model should be developed, encompassing raw material acquisition, synthesis processes, and end-of-life disposal. Additionally, process optimization techniques, such as energy-efficient synthesis methods and waste minimization strategies, should be employed to reduce costs and enhance overall sustainability.

Future advancements in research on CGS-based porous materials will be significantly propelled by the integration of multidisciplinary approaches and technological innovations. Specifically, the integration of novel energy technologies, such as ultrasound and microwave irradiation, during the synthesis process could further enhance fabrication efficiency and environmental sustainability. These technologies are characterized by rapid heating rates, uniform energy distribution, and reduced processing times, thereby improving the overall quality and performance of CGS-based porous materials. Although silicon, aluminum, and carbon in CGS are effectively utilized, other trace elements, such as iron or magnesium, may also hold potential. For instance, CGS-based materials containing iron may exhibit enhanced catalytic activity, while those containing magnesium could offer improved thermal stability. To fully harness the value of CGS and its constituent elements, a comprehensive full-component recovery strategy should be implemented. This strategy aims to recover and utilize not only the major components (silicon, aluminum, carbon) but also the trace elements (iron, magnesium, *etc.*) that are often overlooked. By doing so, we can maximize the resource efficiency of CGS and minimize waste generation. Under global carbon neutrality targets, CGS-based porous materials are poised to find broader applications in catalytic systems, electrochemical devices, and photovoltaic technologies. Their unique properties, including high surface area, tunable porosity, and excellent chemical stability, render them ideal candidates for these applications. By harnessing the potential of these materials, we can contribute to the development of more sustainable and efficient technologies, thus advancing the global pursuit of carbon neutrality.

Data availability

No primary research results, software or code have been included and no new data were generated or analyzed as part of this review.

Author contributions

Writing—original draft preparation, M. H.; and A. G.; writing—review and editing, M. H.; and J. G.; method and visualization, C. H.; and J. Z.; supervision and project administration, J. M.; and J. Z.; funding acquisition, J, M. All authors have read and agreed to the published version of the manuscript.

Conflicts of interest

The authors declare no conflicts of interest.

Acknowledgements

This research was financially supported by the National Key Research and Development Program Project (No. 2022YFC3900100), the National Natural Science Foundation of China (No. U21A20321), and the Shanxi Province Central Government Guided Local Science and Technology Development Fund Project (No. YDZJSX2022A004).

References

1 Z. Xue, C. Yang, L. Dong, W. Bao, J. Wang and P. Fan, *Sep. Purif. Technol.*, 2023, **304**, 122394.
2 S. Su, M. H. Tahir, X. Cheng and J. Zhang, *J. Environ. Chem. Eng.*, 2024, **12**, 112112.
3 X. Guo, Y. Tang, Y. Wang, C. F. Eble, R. B. Finkelman, B. Huan and X. Pan, *J. Cleaner Prod.*, 2021, **280**, 124329.
4 D. Liu, W. Wang, Y. Tu, G. Ren, S. Yan, H. Liu and H. He, *J. Cleaner Prod.*, 2022, **363**, 132426.
5 G. Dai, S. Zheng, X. Wang, Y. Bai, Y. Dong, J. Du, X. Sun and H. Tan, *J. Environ. Manage.*, 2020, **271**, 111009.
6 H. Yaqoob, Y. H. Teoh, T. S. Goraya, F. Sher, M. A. Jamil, T. Rashid and K. A. Yar, *Case Stud. Chem. Environ. Eng.*, 2021, **3**, 100081.
7 Z. Chai, B. Liu, P. Lv, Y. Bai, J. Wang, X. Song, W. Su and G. Yu, *Fuel*, 2023, **333**, 126318.
8 Y. Guo, Y. Zhang, X. Zhao, J. Xu, G. Qiu, W. Jia, J. Wu and F. Guo, *Sci. Total Environ.*, 2022, **831**, 154726.
9 T. Wu, M. Gong, E. Lester, F. Wang, Z. Zhou and Z. Yu, *Fuel*, 2007, **86**, 972–982.
10 Z. Xue, F. Gao, L. Dong, W. Bao, J. Wang and P. Fan, *J. Environ. Chem. Eng.*, 2023, **11**, 110653.
11 Y. Chen, X. Zhou, S. Wan, R. Zheng, J. Tong, H. Hou and T. Wang, *Constr. Build. Mater.*, 2019, **211**, 646–658.
12 F. Luo, Y. Jiang and C. Wei, *Constr. Build. Mater.*, 2021, **269**, 121259.
13 Z. Li, Y. Zhang, H. Zhao, H. Chen and R. He, *Constr. Build. Mater.*, 2019, **213**, 265–274.
14 X. Liu, Z. Jin, Y. Jing, P. Fan, Z. Qi, W. Bao, J. Wang, X. Yan, P. Lv and L. Dong, *Chin. J. Chem. Eng.*, 2021, **35**, 92–106.
15 Y. Guo, F. Guo, L. Zhou, Z. Guo, Z. Miao, H. Liu, X. Zhang, J. Wu and Y. Zhang, *Fuel*, 2021, **292**, 120387.
16 D. Zhu, S. Miao, B. Xue, Y. Jiang and C. Wei, *Water, Air, Soil Pollut.*, 2019, **230**, 155.
17 T. Liu, M. Kumar Awasthi, M. Jiao, S. Kumar Awasthi, S. Qin, Y. Zhou, H. Liu, J. Li and Z. Zhang, *Bioresour. Technol.*, 2021, **325**, 124703.
18 W. Ai, S. Liu, J. Zhang, S. Miao and C. Wei, *J. Appl. Polym. Sci.*, 2019, **136**, 47803.
19 Y. Tang, H. Yin, H. Yuan, H. Shuai and Y. Xin, *Adv. Powder Technol.*, 2016, **27**, 2232–2237.
20 Q. Guo, H. Li, S. Wang, Y. Gong, L. Ren and G. Yu, *Chem. Eng. J.*, 2022, **446**, 137256.
21 B. Lv, X. Deng, F. Jiao, B. Dong, C. Fang and B. Xing, *Process Saf. Environ. Prot.*, 2023, **171**, 859–873.
22 F. Guo, Z. Miao, Z. Guo, J. Li, Y. Zhang and J. Wu, *Fuel*, 2020, **267**, 117043.
23 J. Wang, L. Kong, J. Bai, K. Xue, X. Zhu, Y. Luo, X. Zhao, H. Li, Z. Guo, Z. Bai and W. Li, *Fuel*, 2021, **292**, 120390.
24 P. Grammelis, N. Margaritis and E. Karampinis, in *Fuel Flexible Energy Generation*, 2016, pp. 29–58.
25 S. Dong, J. Qiao, C. Kang, M. Sun, S. Yang, Y. Zhao, Y. Yang, W. Sun and C. Duan, *Sep. Purif. Technol.*, 2025, **367**, 132800.
26 Y. Cao, C. Zhou, F. Gao, Y. Huang, W. Zhu, G. Liu and J. Wang, *Chem. Eng. J.*, 2024, **498**, 155121.
27 L. Gui, Z. Zhang, K. Sun, X. Shi, S. Liang, H. Duan, Z. Yang, S. Yuan, L. Guo, J. Xu and J. Yang, *J. Environ. Chem. Eng.*, 2024, **12**, 112970.
28 M. Yang, Y. Li, X. Shi, N. Fen, L. Ma, W. Ji, Y. Xiao, K. Shi, Y. Sun, Y. Li and Y. Ma, *Microporous Mesoporous Mater.*, 2025, **383**, 113410.
29 F. Liu, M. Xie, G. Yu, C. Ke and H. Zhao, *ACS Sustain. Chem. Eng.*, 2021, **9**, 10318–10325.
30 M. Lu, Z. Xiong, K. Fang, X. Li, J. Li and T. Li, *Renewable Energy*, 2020, **160**, 385–395.
31 R. Wang, Y. Song, X. Yang, J. Zhou, Q. Jiang, Z. Wang, L. Wang, B. Peng, H. Song and W. Lin, *ACS Sustain. Chem. Eng.*, 2022, **10**, 11376–11386.
32 J. Guo, H. Wu, Y. Wei, Y. Miao, J. Qu and P. Wang, *RSC Adv.*, 2024, **14**, 1686–1696.
33 G. K. R. Angaru, L. P. Lingamdinne, Y. L. Choi, J. R. Koduru, J. K. Yang and Y. Y. Chang, *Mater. Today Chem.*, 2021, **22**, 100577.
34 S. Wu, S. Huang, L. Ji, Y. Wu and J. Gao, *Fuel*, 2014, **122**, 67–75.
35 Z. Xue, Y. Feng, H. Li, C. Xu, J. Ju, L. Dong, C. Yang, W. Bao, J. Wang, H. Wang and R. Ma, *Fuel*, 2023, **348**, 128508.
36 T. Matamba, S. Iglauer and A. Keshavarz, *J. Energy Inst.*, 2022, **105**, 81–102.
37 Z. Xu, Y. Wang, Y. Qian, J. Zhang, Y. Tu, S. Gu and M. Sun, *Sep. Purif. Technol.*, 2025, **361**, 131517.
38 C. Li, R. Liu, J. Zheng, L. Liao and Y. Zhang, *Int. J. Hydrogen Energy*, 2022, **47**, 12528–12538.
39 Y. Guo, H. Li, G. Qiu, Y. Li, Y. Niu, J. Xu, W. Jia, Y. Zhang, J. Wu and F. Guo, *Sep. Purif. Technol.*, 2023, **306**, 122675.
40 P. Jiang, C.-r. Xie, C.-l. Luo, W. Meng, G. Yang, G.-s. Yu, Y. Gong, M. Xu and T. Wu, *Fuel*, 2021, **303**, 121163.
41 W. Zhang, S. Huang, S. Wu, Y. Wu and J. Gao, *Fuel*, 2019, **254**, 115699.
42 J. Qu, J. Zhang, H. Li and S. Li, *Sci. Total Environ.*, 2021, **801**, 148761.
43 Z. Miao, L. Chen, K. Chen, X. Zhang, Y. Zhang and J. Wu, *Adv. Powder Technol.*, 2020, **31**, 3781–3789.
44 Z. Miao, J. Wu, Y. Zhang, X. Zhao, F. Guo, Z. Guo and Y. Guo, *Energy Fuel.*, 2019, **34**, 616–623.
45 L. Zhou, Q. Ren, C. Liang, W. Wang and W. Li, *Energy*, 2023, **272**, 127190.
46 J. Zhang, J. Zuo, Y. Jiang, D. Zhu, J. Zhang and C. Wei, *Solid State Sci.*, 2020, **100**, 106084.
47 S. Wu, S. Huang, Y. Wu and J. Gao, *J. Energy Inst.*, 2015, **88**, 93–103.
48 J. Li, S. Fan, X. Zhang, Z. Chen, Y. Qiao, Z. Yuan, L. Zeng and Z. Li, *Energy*, 2022, **251**, 123930.
49 Y. Yang, M. Chu, X. Shi, F. Lyu, X. Sun and C. Jia, *ACS Omega*, 2020, **5**, 26883–26893.
50 Y. Tang, X. Guo, Q. Xie, R. B. Finkelman, S. Han, B. Huan and X. Pan, *Energy Fuel.*, 2018, **32**, 3052–3067.
51 S. Wang, X. Gu, J. Liu, Z. Zhu, H. Wang, X. Ge, Z. Hu, X. Xu, M. L. Nehdi and X. Wang, *Constr. Build. Mater.*, 2024, **450**, 138764.
52 J. Zhang, J. Zuo, W. Ai, S. Liu, D. Zhu, J. Zhang and C. Wei, *J. Hazard. Mater.*, 2020, **384**, 121347.

53 D. Zhu, J. Zuo, Y. Jiang, J. Zhang, J. Zhang and C. Wei, *Sci. Total Environ.*, 2020, **707**, 136102.
54 Z. Miao, J. Xu, L. Chen, R. Wang, Y. Zhang and J. Wu, *Fuel*, 2022, **309**, 122334.
55 S. Liu, J. Wei, X. Chen, W. Ai and C. Wei, *Arabian J. Sci. Eng.*, 2020, **45**, 4647–4657.
56 M. Du, J. Huang, Z. Liu, X. Zhou, S. Guo, Z. Wang and Y. Fang, *Fuel*, 2018, **224**, 178–185.
57 W. Zhang, S. Xiong, J. Cheng, Y. Zhang, X. Zhao, N. Yang, F. Lv, X. Wang, C. Wang and Z. Li, *ACS Appl. Electron. Mater.*, 2024, **6**, 1781–1789.
58 X. You, L. Song, J. Wang, J. Lv, L. Sun, L. Li and M. He, *J. Water Process Eng.*, 2024, **63**, 105488.
59 R. Han, A. Zhou, N. Zhang, Z. Li, X. Chen, T. Nan and Z. Zhang, *Chem. Eng. Sci.*, 2025, **310**, 121532.
60 D. Lozano-Castelló, J. M. Calo, D. Cazorla-Amorós and A. Linares-Solano, *Carbon*, 2007, **45**, 2529–2536.
61 Z. Miao, Z. Guo, G. Qiu, Y. Zhang and J. Wu, *J. CO_2 Util.*, 2021, **50**, 101585.
62 L. Xu, K. Dong, F. Guo, S. Liu, Q. Qiao, S. Mao, L. Qian and Y. Bai, *Energy*, 2023, **274**, 127294.
63 A. Ahmadpour and D. D. Do, *Carbon*, 1996, **34**, 471–479.
64 Y. Kang, X. Wei, G. Liu, M. Mu, X. Ma, Y. Gao and Z. Zong, *Chin. J. Chem. Eng.*, 2020, **28**, 1694–1700.
65 H. Zhang, J. Niu, Y. Guo and F. Cheng, *Fuel*, 2021, **287**, 119481.
66 Y. Huang, F. Bao, J. Wang, Z. Gu, H. Zhang, J. Wang, J. Dan, Y. Liao, C. Hong and J. Liu, *Sep. Purif. Technol.*, 2025, **353**, 128397.
67 Z. Li, Y. Chen, D. Wang, K. Yang and J. Sun, *Appl. Surf. Sci.*, 2025, **679**, 161186.
68 Y.-y. Gu and X.-c. Qiao, *Microporous Mesoporous Mater.*, 2019, **276**, 303–307.
69 Z. Miao, X. Han, H. Ge, R. Wu, C. Zhang, H. Zhu and S. Wang, *Sep. Purif. Technol.*, 2024, **339**, 126540.
70 B. Liu, Z. Chai, P. Lv, Y. Bai, J. Wang, Q. Guo, W. Su and G. Yu, *Fuel*, 2023, **346**, 128318.
71 B. Liu, P. Lv, Q. Wang, Y. Bai, J. Wang, W. Su, X. Song and G. Yu, *J. Environ. Chem. Eng.*, 2024, **12**, 112635.
72 Y. Tang, L. Li, K. Yang, C. Wang, P. Yang, L. Dong, F. Zhao and Z. Fang, *Microporous Mesoporous Mater.*, 2025, **392**, 113627.
73 B. Lv, W. Fan, F. Jiao, Y. Jiao and B. Xing, *J. Environ. Chem. Eng.*, 2025, **13**, 116298.
74 M. Habib, T. Ayaz, M. Ali, M. Zeeshan, X. Sheng, R. Fu, S. Ullah and S. Lyu, *J. Environ. Manage.*, 2024, **365**, 121441.
75 Y. Wang, Z. Xu, Y. Tu, S. Gu, Z. Su and Z. Peng, *J. Environ. Chem. Eng.*, 2024, **12**, 113805.
76 X. Shi, L. Xu, J. Tian, K. Shu, Z. Wang, K. Xue, H. Wu, D. Wang and G. Li, *J. Water Process Eng.*, 2025, **69**, 106670.
77 L. Jia, H. Li, M. Sun, X. Liu, H. Zhang, M. Zou, Z. Guo, Z. Fu and S. Zeng, *Sep. Purif. Technol.*, 2025, **368**, 133049.
78 X. Hai, B. Ma, Q. Wang, X. Liu, L. Ma, Y. Bai, P. Lv, X. Song and G. Yu, *J. Environ. Manage.*, 2025, **382**, 125290.
79 J. Zhang, Y. Liu, J. Zhang, J. Zuo, J. Zhang, F. Qiu, C. Wei and S. Miao, *Powder Technol.*, 2021, **386**, 437–448.
80 W. Ai, Y. Li, X. Zhang, L. Xiao and X. Zhou, *Environ. Sci. Pollut. Res.*, 2022, **29**, 88894–88907.
81 W. Ai, J. Zhang, J. Zhang, S. Miao and C. Wei, *J. Appl. Polym. Sci.*, 2019, **137**, 48601.
82 Y. Zhang, D. Ma, X. Men, W. Chen and S. Gao, *Mater. Res. Bull.*, 2024, **174**, 112720.
83 Y. Zhang, S. Gao, X. Zhang, D. Ma, C. Zhu and J. He, *Int. J. Miner., Metall. Mater.*, 2024, **32**, 221–232.
84 B. Liu, P. Lv, R. Wu, Y. Bai, J. Wang, W. Su, X. Song and G. Yu, *Sep. Purif. Technol.*, 2023, **323**, 124478.
85 Y. Xu and X. Chai, *Environ. Technol.*, 2017, **39**, 382–391.
86 S. Yang, G. Fan, L. Ma, C. Wei, P. Li, Y. Cao and D. Teng, *Molecules*, 2024, **29**, 5232.
87 B. Lv, X. Deng, F. Jiao, B. Dong, C. Fang and B. Xing, *Process Saf. Environ. Prot.*, 2023, **174**, 869–881.
88 K.-b. Cui, J.-w. Lyu, H.-z. Liu, J.-l. Yang, Z.-q. Yan, W. Yang, X. Liu and J. Qiu, *J. Environ. Chem. Eng.*, 2024, **12**, 113739.
89 Y. Niu, L. Chen, S. Guo, J. Xu, H. Li, F. Guo, Y. Zhang and J. Wu, *Fuel*, 2024, **358**, 130139.
90 R. Shu, Q. Qiao, F. Guo, K. Dong, S. Liu, L. Xu, Y. Bai and N. Zhou, *Environ. Res.*, 2023, **217**, 114912.
91 Y. Long, P. Yang, C. Wang, W. Wu, X. Chen, W. Liu, Z. Cao, X. Zhan, D. Liu and W. Huang, *Chem. Eng. J.*, 2023, **456**, 140996.
92 C. Sun, H. Pan, T. Shen, J. Sun, S. He, T. Li and X. Lu, *RSC Adv.*, 2024, **14**, 4890–4903.
93 W. Ji, S. Zhang, P. Zhao, S. Zhang, N. Feng, L. Lan, X. Zhang, Y. Sun, Y. Li and Y. Ma, *Appl. Sci.*, 2020, **10**, 2694.
94 B. Yang, F. Han, Z. Xie, Z. Yang, F. Jiang, S. Yang and Y. Li, *RSC Adv.*, 2022, **12**, 17147–17157.
95 Z. Miao, J. Wu, G. Qiu, Z. Guo, X. Zhao and Y. Zhang, *Sci. Total Environ.*, 2022, **821**, 153347.
96 Z. Miao, G. Qiu, X. Zhao, F. Guo, Y. Zhang and J. Wu, *J. CO_2 Util.*, 2021, **54**, 101754.
97 J. Zhang, J. Zuo, W. Ai, J. Zhang, D. Zhu, S. Miao and C. Wei, *Appl. Surf. Sci.*, 2021, **537**, 147938.
98 Y. Zhu, J. Wu, Y. Zhang, Z. Miao, Y. Niu, F. Guo and Y. Xi, *Sep. Purif. Technol.*, 2024, **330**, 125452.
99 X. Wei, J. Liu, H. Yan, T. Li, Y. Wang, Y. Zhao, G. Li and G. Zhang, *Sep. Purif. Technol.*, 2025, **353**, 128348.
100 Y. Zhang, H. Li, S. Gao, Y. Geng and C. Wu, *Asia-Pac. J. Chem. Eng.*, 2019, **14**, e2336.
101 W. Wang, W. Li, Q. Ren and Q. Lyu, *Energy*, 2024, **293**, 130714.
102 S. Gao, C. Wu, Y. Zhang and H. Li, *Ceram. Int.*, 2021, **47**, 4994–5002.
103 J. He, S. Gao, Y. Zhang and H. Li, *J. Alloys Compd.*, 2021, **874**, 159878.